Seismicity-constrained fault detection and characterization with a multitask machine learning model

Kai Gao*[,1] and Ting Chen[1]

[1]Earth and Environmental Sciences Division, Los Alamos National Laboratory, Los Alamos, NM 87545, USA

This is a non-peer-reviewed preprint submitted to *EarthArXiv* for public posting. The manuscript has been submitted to *Journal of Geophysical Research: Machine Learning and Computation* for peer review. Its structure and content may change with the peer-review process.

*Corresponding author; Email: kaigao@lanl.gov

Abstract

Geological fault detection and characterization from geophysical data have been one of the center challenges in geophysics and seismology as it holds the key to understanding subsurface dynamics ranging from borehole, reservoir, to regional scales. While paradigms of auto or semi-auto fault delineation either based on seismicity location analysis or on seismic migration image reflector discontinuity identification have been well established, a systematic method that can integrate both seismic image and seismicity location information is still missing. We develop a novel machine learning (ML) model that integrates seismic reflector image and seismicity location information into a unified model to automatically identify geological faults and characterize their geometrical properties. We detail the architecture of this neural network, the strategy and procedure of high-quality training data-label generation, as well as the validation results on the trained models. Specially, we also use two field data examples to validate the efficacy and accuracy of our ML model. The results demonstrate that by integrating seismicity location information and seismic migration image in a unified framework, the end-to-end neural network provides notably higher fidelity in delineating subsurface faults and its geometrical properties compared with image-only fault detection methods.

Plain Language Summary

Geological fault detection and characterization are essential to understanding a variety of geophysical and seismological processes, ranging from subsurface fluid migration, anthropogenic microearthquakes, to natural earthquakes. By integrating seismicity location and seismic migration image into a unified framework, we develop an end-to-end, multitask machine learning model for recognizing geological faults with a high fidelity and high resolution. We demonstrate the efficacy and accuracy of our seismicity-constrained fault detection machine learning model with both synthetic and field data examples. The method can serve as a powerful tool for subsurface characterization and seismic hazards mitigation.

1 Introduction

Geological faults and fractures at different scales are key to understanding subsurface geomechanical state and geodynamical processes. For fossil energy exploration, geological faults create structural traps and migration channels for controlling oil and gas accumulation (Manzocchi et al., 2010). For clean energy reservoirs such as geothermal reservoirs, faults are critical channels for geothermal fluid circulation and heat extraction (Gao et al., 2021). Accurately mapping faults is critical to evaluating the energy capacity and operation safety. From a seismogenic point of view, faults are the fundamental cause of natural earthquakes (Aki, 1972; Aki and Richards, 2002). A precise mapping of faults can play an essential role in understanding historical earthquakes and also predict the potential of quakes and seismic hazards, to some extent. Mapping faults is also one of the most important tasks to characterize and understand reservoir-scale anthropogenic microearthquakes (MEQs), a phenomenon caused by excessive fluid injection into a closed to semi-closed subsurface reservoir system (Ellsworth, 2013; Chang and Segall, 2016; Glubokovskikh et al., 2022).

Conventionally, one can identify faults from a seismicity location map or from a seismic migration image.

Locating earthquakes and MEQs to their spatial origin position based on traveltime (e.g., Waldhauser and Ellsworth, 2000) or waveform correlation and stacking (e.g., Schuster et al., 2004; Nakata and Beroza, 2016) can result in a seismicity location map (Li et al., 2020). Clustering of seismicity based on their spatial location can generate fault maps (e.g., Dichiarante et al., 2021; Park et al., 2022). When a number of seismicity form some clearly identifiable spatial pattern, it is straightforward to cluster them into the same group. However, when the seismicity is associated with a complex, intersecting fault network, clustering can become unstable and can be sensitive to the choice of hyper-parameters, and different clustering methods can produce vastly different results (Rodriguez et al., 2019). In such cases, one usually needs to postprocess (sometimes even manually) clustered seismicity to obtain interpretable fault maps (Park et al., 2022). When there exist uncertainties in seismicity location due to, for instance, noise, phase pick error, and/or velocity model inaccuracy, accurately delineating faults from seismicity location may become extremely challenging.

One can also identify faults by locating lateral discontinuities of reflectors on seismic migration image. Early works of automated fault identification focus on computing various fault-related attributes to extract faults, including semblance (Marfurt et al., 1998; Hale, 2013), coherence (Marfurt et al., 1999), entropy (Cohen et al., 2006), and so on. Pedersen et al. (2002) developed the ant-tracking method to search and merge discontinuous regions into fault surfaces. Wu (2017) used local image coherence computed from directional structure tensors to estimate fault likelihood; the underlying principle was later adopted in nonlinear anisotropic diffusion to detect faults and enhance reflector image (Wu and Guo, 2018). Wu and Fomel (2018) developed an optimal surface voting approach for extracting fault attributes. However, some of these methods are of low resolution, and many of them require subjective parameter tuning that varies from image to image. This, sometimes, inevitably introduces human biases. In addition, these methods could easily fail when a given seismic image is of poor quality – in practice, seismic images can contain evident random or coherent noises due to, for instance, unbalanced or sparse source-receiver geometry and limitations in migration algorithms.

Fault detection from seismic image is becoming fully automatic thanks to many machine learning (ML) models. Related works have grown into a large repository that is beyond the scope of this paper to perform a complete review. Xiong et al. (2018) developed a convolutional neural network (CNN) to infer fault probability directly from seismic image patches; the method is essentially an application of CNN-based classification (LeCun et al., 1998). Leveraging the multi-layer perceptron model, Di et al. (2018) developed a semi-supervised patch-level classification neural network to infer fault probability from multiple seismic image and fault attributes. Wu et al. (2019a) recognized that fault detection on a seismic image is analogous to medical image segmentation, and developed a simplified U-Net (Ronneberger et al., 2015), namely FaultSeg3D, for end-to-end fault detection. The input is a single seismic migration image, while the output is a map where each pixel represents the probability of the pixel being a fault pixel. FaultSeg3D provides the first end-to-end approach to detect faults directly from seismic images, significantly automating and improving the accuracy of fault detection. An et al. (2021) improved the performance of deep CNNs for fault recognition by an expert-labeled fault dataset; the results also indicate the importance of high-quality training data for fault detection task (Cunha et al., 2020). Gao et al. (2022a) developed a nested residual U-Net to improve the performance of end-to-end fault detection. Gao et al. (2022b) developed a multiscale fusion fully convolutional NN to combine encoded image features at different spatial scales for improving fault detection. An et al. (2023) conducted a comprehensive review of ML-based fault detection emerged in recent years.

The emergence of the so-called transformer model from the natural language processing domain (Vaswani et al., 2017) provides a strong mechanism, attention, to capturing long-distance and global relation of sequence. This inspired the vision transformer (ViT) (Dosovitskiy et al., 2021) in the computer vision domain. Under this paradigm, many pure ViT, improved ViT, or mixed ViT-CNN/U-Net models (e.g., Liu et al., 2021; Chen et al., 2024) can be used for fault detection. For instance, Wang et al. (2024b) developed a fault detection architecture based on by refining the self attention mechanism in transformer/ViT with a fast global self attention module to produce improved fault detection. Wang et al. (2024a) compared several different ML models for fault detection, and noted that convolutional NNs (CNNs) are generally computationally efficient, but performs weaker than ViT based NNs in delineating long, continuous faults they lack a fundamental mechanism to properly capture long-distance or global relation of the input seismic image. However, because transformers cannot inherently learn the inductive bias of image features, ViT-based fault detection NNs requires a huge amount of data-labels to train, which could be a major challenge for the fault detection task unless the data are purely synthetic. In general, in these existing ML models, one feed a 2D or 3D seismic image into a neural network (NN) that consists of convolutional blocks and/or vision transformers, and obtain a so-called fault probability map corresponding to the image. On the basis of these works, Bi et al. (2021) developed a multitask NN to simultaneously infer relative geological time and faults from a seismic image. Wu et al. (2023) developed a multitask NN for fault detection, where in addition to the main task (fault detection), they introduced an auxiliary task (seismic image reconstruction) to provide additional constraints and information for the main task. Yang et al. (2023) developed a transformer-based multitask learning model to simultaneously learn and infer relative geological time and fault probability from a seismic image. Gao (2024) developed a multitask iterative NN to infer multiple geological features, including higher-resolution reflectivity image, relative geological time, and multiple fault attributes (probability, strike and dip), from a single seismic image. This is the first multitask NN that demonstrates the feasibility of inferring the geometrical attributes of faults in end-to-end fashion on a pixel level, in contrast to previous works (e.g., Xiong et al., 2018; Wu et al., 2019c) that infer these fault attributes in a classification fashion. Further, recognizing the challenge that ML models may generate scattered, discontinuous faults, Gao (2024) develops an iterative refinement strategy to improve the interpretability of the inferred images, relative geological time, and fault attributes. All of these works extended the frontiers of ML-based automatic fault detection and characterization, a domain that embraces novel methods and algorithms frequently. However, we recognized that all these methods have focused on developing new architectures to improve the learning and inference from a seismic migration image.

However, the two aforementioned paradigms (i.e., image-based fault detection and seismicity-location-based fault delineation) are mostly independent with each other, and there has not been a systematic mechanism to integrate them into a unified framework to jointly characterize faults, especially in the regime of ML. This is partially because seismic image and seismicity location map have essentially different characteristics in space.

Motivated by this challenge, we develop a novel end-to-end, multitask ML model for identifying faults using both seismic migration image and seismicity location information. The input to this NN includes a seismic migration image and a source image (a discrete representation of seismicity locations), and the output includes multiple fault attributes, including fault probability, fault dip, and fault strike, on a pixel/voxel level. This architecture means that our NN does not contain any classification or regression. Instead, it transforms the estimation of fault attributes into a direct end-to-end mapping problem using fully convolutional NN. Our NN transforms the input through a number of encoders and decoders, where each of the encoders or decoders is a simplified U-Net with a residual connection. To effectively extract and learn the features embedded in the migration image and the source image, we use two independent encoder branches to learn the two input images, and merge the feature maps into the same encoder before decoding. The NN provides a systematic mechanism to leverage both migration image and seismicity location for fully automatic fault detection and characterization. Moreover, to apply our NN to elastic migration images, we develop a systematic algorithm to generate synthetic elastic migration images, and find that it can provide a systematic method to use PP, PS, SP, and SS migration images simultaneously for fault detection, if such images are available for a region. Along with the details of this new NN, we elaborate the method of preparing realistic source images as part of the input data. To the best of our knowledge, our model is the first ML model that leverages information from both seismic image and seismicity location for fully automatic, multitask fault characterization, representing a novel paradigm in high-fidelity fault detection and characterization. We thus name it a seismicity-constrained fault characterization neural network, or SCF-Net for convenience.

The rest of the paper is organized as following: In the "Methodology" section, we detail the architecture of our ML model, the methods and algorithms for generating training data and labels, and the training strategy. We validate our trained ML model and compare it with a conventional ML fault detection model to demonstrate the advantage. In the "Results" section, we use two field data examples to demonstrate the efficacy and accuracy of our seismicity-constrained fault characterization neural network. We then summarize our methods and results in "Conclusions."

2 Methodology

2.1 Architecture

We display the architecture of our multitask seismicity-constrained fault detection and characterization neural network (NN) in Figure 1. Denoting an input image as I of size $N_1 \times N_2 \times N_3$ and an source image as S of the same size, we construct the encoder branches of SCF-Net as

$$
\begin{aligned}
E_I^1 &= \mathcal{R}^1_{c=1\to16}(I), && (1)\\
E_S^1 &= \mathcal{R}^1_{c=1\to16}(S), && (2)\\
E_I^2 &= \mathcal{R}^2_{c=16\to32} \circ \mathcal{M}_{k=2}(E_I^1), && (3)\\
E_S^2 &= \mathcal{R}^2_{c=16\to32} \circ \mathcal{M}_{k=2}(E_S^1), && (4)\\
L &= \mathcal{R}^3_{c=32+32\to64} \circ \mathcal{M}_{k=2}(E_I^2 \oplus E_S^2), && (5)
\end{aligned}
$$

and the decoder branch as

$$
\begin{aligned}
D_2 &= \mathcal{R}^2_{c=32\times2+64\to32}(\mathcal{U}_{k=2}(L) \oplus E_I^2 \oplus E_S^2), && (6)\\
D_1 &= \mathcal{R}^2_{c=16\times2+32\to16}(\mathcal{U}_{k=2}(D_2) \oplus E_I^1 \oplus E_S^1), && (7)
\end{aligned}
$$

where $\mathcal{M}_{k=2}$ represents a max-pooling layer with a kernel size of 2 (Murphy, 2022), $\mathcal{U}_{k=2}$ represents a bilinear/trilinear upsampling layer with a scaling ratio of 2, and $\mathcal{R}^1$, $\mathcal{R}^2$, and $\mathcal{R}^3$ represent small U-Nets with residual connections (ResUNet) (Qin et al., 2020; Gao et al., 2022a). The architectures of these ResUNets are detailed in Figure 2a-c, respectively. The subscripts $c = a \to b$ in these symbols represent the numbers of input and output channels associated with these ResUNets, following a notation convention in PyTorch (Paszke et al., 2019), the library used for implementing our seismicity-constrained fault NN and other relevant NNs in this paper.

Following the output from D_1, we obtain the fault probability as

$$F_0 = \mathcal{C}_{c=16\to16} \circ \mathcal{C}_{c=16\to16} \circ \mathcal{C}_{c=16\to16} \circ \mathcal{C}_{c=16\to16}(D_1), \tag{8}$$

$$F_p = \mathcal{S} \circ \mathcal{C}'_{c=16\to1} \circ \mathcal{C}_{c=32\to16} \circ \mathcal{C}_{c=32\to32} \circ \mathcal{C}_{c=32\to32} \circ \mathcal{C}_{c=16\to32}(F_0), \tag{9}$$

while the fault dip and strike maps are inferred with two additional "subdecoders" as

$$F_d = F_p \otimes \left[\mathcal{S} \circ \mathcal{C}_{c=16\to1} \circ \mathcal{C}_{c=32\to16} \circ \mathcal{C}_{c=32\to32} \circ \mathcal{C}_{c=32\to32} \circ \mathcal{C}_{c=16\to32}(F_0)\right], \tag{10}$$

$$F_s = F_p \otimes \left[\mathcal{S} \circ \mathcal{C}_{c=16\to1} \circ \mathcal{C}_{c=32\to16} \circ \mathcal{C}_{c=32\to32} \circ \mathcal{C}_{c=32\to32} \circ \mathcal{C}_{c=16\to32}(F_0)\right], \tag{11}$$

where $\mathcal{C}_{c=a\to b}$ represents a composite operation of a convolutional layer with an input channel number of a and an output channel number of b, an instance normalization layer (Ulyanov et al., 2016), followed by a rectified linear unit (ReLU) layer (Murphy, 2022); for F_p, the final $\mathcal{C}'$ does not include an instance normalization layer. The symbol $\mathcal{S}$ represents a sigmoid activation function which transforms any input to the range of $[0, 1]$ (Murphy, 2022). The symbol "$\circ$" represents composition of functions and "$\otimes$" represents pixel-wise multiplication.

The architecture indicates that our NN does not simply treat the attributes of faults as different channels of a feature map. Instead, the inference of multiple fault attributes is based on different "subdecoders," like multiple partially independent tasks.

By contrast, conventional fault detection NNs only use a seismic migration image to infer fault probability attribute based on, for instance, a U-Net (Wu et al., 2019b), a nested residual U-Net (NRU-net) (Gao et al., 2022a), or more recent ViT (Wang et al., 2024b). To ensure a fair comparison in the following examples, we build a migration-image-only NN by removing the source image encoder branch (and any associated concatenation) from the architecture displayed in Figure 1 to obtain fault attributes. To distinguish the two ML models, we name them "F-Net" (Fault-Net) and "SCF-Net" (Seismicity-Constrained Fault-Net), respectively. We also develop an SCF-Net for elastic migration images as detailed in Appendix A. For simplicity, we name it "elastic SCF-Net" to distinguish it from the SCF-Net for a single migration image.

2.2 Training data preparation

Generating high-quality and high-fidelity synthetic seismic images, source images, and fault labels is critical to our ML model, as we only use synthetic data to train the NN and apply the

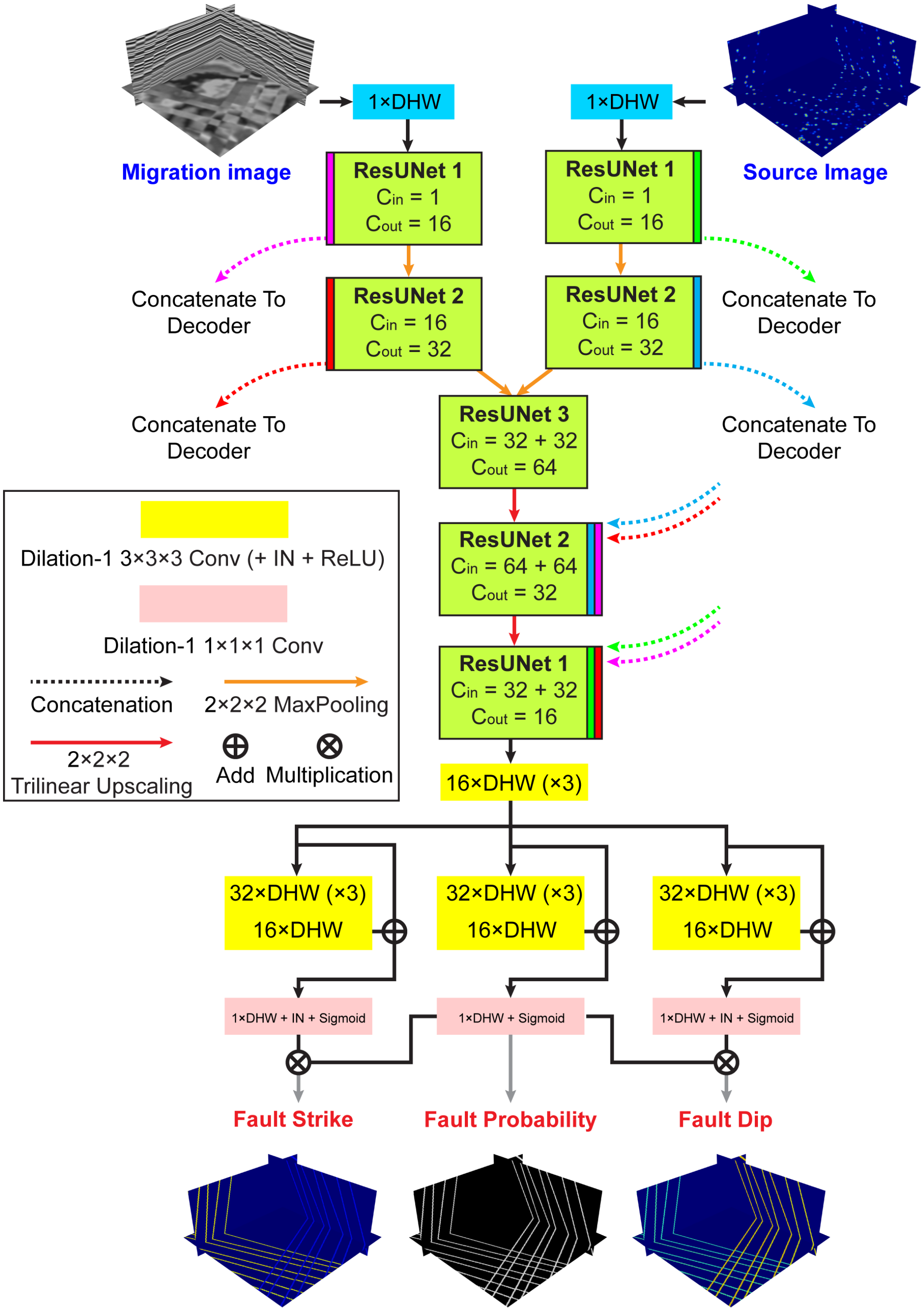

Figure 1: Architecture of our end-to-end seismicity-constrained fault characterization neural network (SCF-Net). "ResUNet" stands for small residual U-Net. The input (including acoustic or elastic migration images and a source image) and the output (including fault probability, dip, and strike) are all regularly sampled images of the same dimension. The methodology for converting seismicity location to a regular-grid source image is detailed in the text.

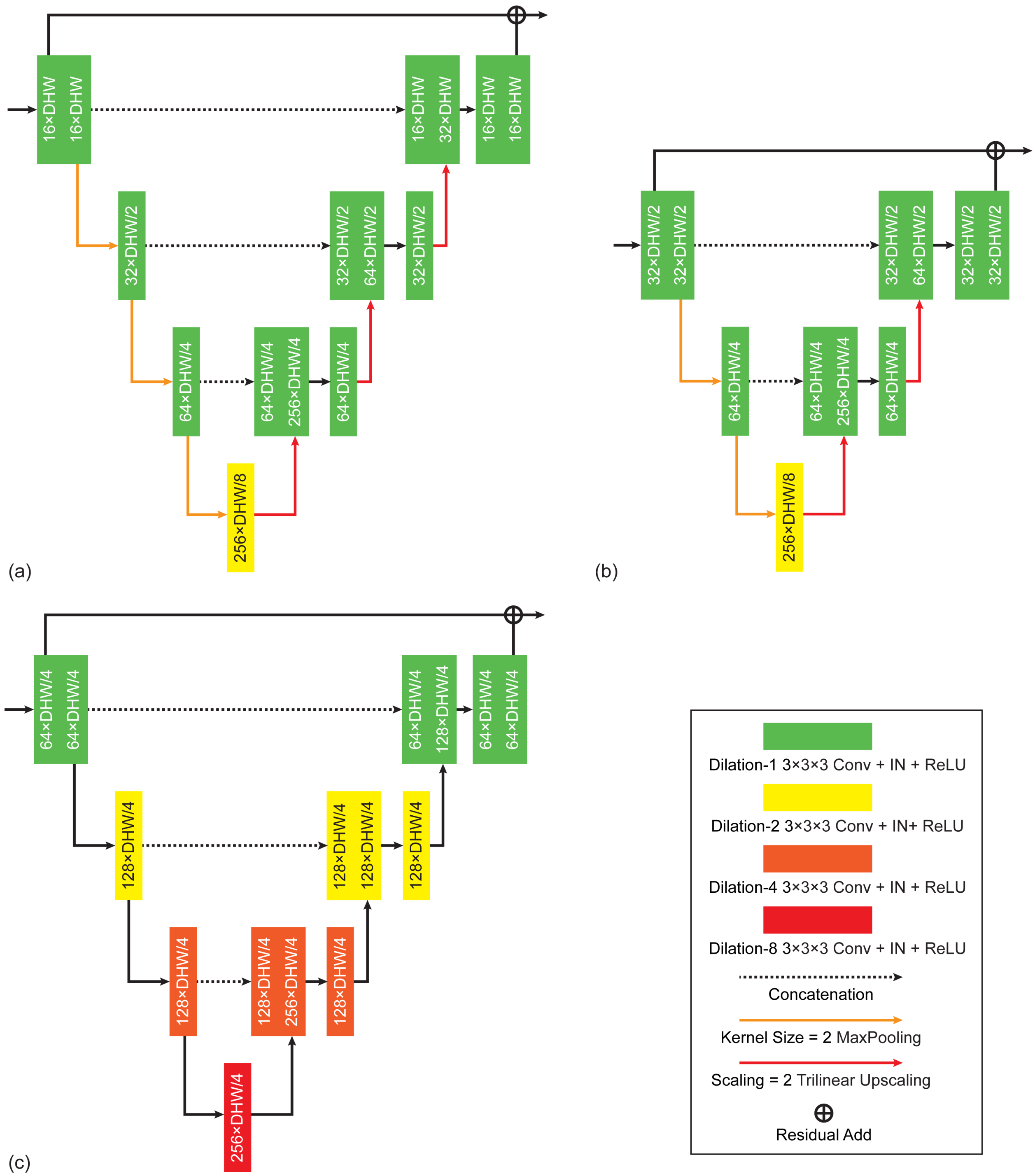

Figure 2: Architecture of ResUNets for constructing SCF-Net displayed in Figure 1. Different colors in these ResUNets represent convolutional blocks with different dilation ratios. Panels (a-c) correspond to ResUNet-1, 2, and 3 in Figure 1, respectively. Numbers in the convolutional layers are number of channels.

trained model to field data images without further training. The strategy may not produce optimal results for every field data image, but requires much less effort in preparing training data-labels.

To generate realistic seismic migration images and fault labels, we first generate a 1D random, sparse seismic reflectivity series of length N_1, stack $N_2 \times N_3$ of such reflectivity horizontally to obtain a 3D image volume, and then randomly shift the 1D traces up and down to generate lateral variations. We then insert N_f random faults with random dip, strike, and rake into the image. For each fault, we shift one of the two blocks on two sides of the fault upwards or downwards with a random displacement. For different images, the number of nonzero reflectivity coefficients (or equivalently, the number of layers) and the number of faults can be different. For some of the images, we also insert unconformity at the top to mimic sedimentary unconformity in reality. Note that in practice, geological unconformity can form low or even ultra-low intersection angles with underlying sedimentary layers, making it challenging to distinguish them from low-angle faults, if any, on the seismic image, as both of them appear as lateral discontinuities of reflectors. We recognize that this is an open question and beyond the scope of this paper. Our future work may develop a solution to distinguish the two geological features. In the process, we obtain multiple labels corresponding to the attributes of faults, including probability, dip, strike, rake, and displacement. In this work, we focus on inferring fault dip and strike attributes from an input image.

To generate a source image corresponding to a seismic migration image, we assign random source locations that are close to the generated faults by setting an upper limit of the distance of source locations to faults, as displayed in Figure 3. Each source is represented by a Gaussian function projected on the same regular grid as the seismic image. Because different sources may overlap, we use a maximum-limiting Gaussian function summation to compute the source location probability at spatial location $\mathbf{x}$ as

$$S(\mathbf{x}) = \max_{i=1,2,\cdots,N;\mathbf{x}_i \in R_1} \exp\left(-\frac{\|\mathbf{x}-\mathbf{x}_i\|^2}{2\sigma^2}\right), \tag{12}$$

where $\mathbf{x}_i$ represents the location of the i-th source associated with this image. We choose $1/2\sigma^2 = 0.3$ in this work. This indicates that the maximum value of the source image is 1, and the probability of a source location will diminish effectively to 0 approximately 4 or 5 grid points away from $\mathbf{x}_i$.

The random distance of source location to a nearby fault varies from source to source, and the number of sources N varies from image to image. This multi-randomization strategy generates the maximum randomness as we can achieve for the source images. In practice, not all parts of faults are associated with seismicity. Therefore, we create a random binary mask R for each image, and only the random sources that fall within nonzero mask regions R_+ of the mask R contribute to the final source image.

We enclose the above algorithm for generating 2D and 3D synthetic images, fault attribute labels,

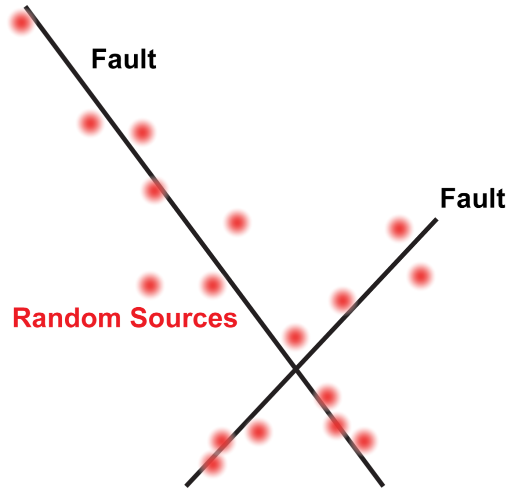

Figure 3: A schematic on the generation of a random source image. The black lines represent faults, while the red clouds represent random sources computed based on equation (12).

as well as source images in the open-source codes associated with this work. The implementation is based on the modules developed in our random geological modeling package, `RGM` (Gao and Chen, 2024). To train the 2D NNs, we generate a total of 6,000 data-label paris, with an additional 600 data-label pairs for validation. These two datasets are not overlapping with each other. Each image (or label) contains $N_1 \times N_2 = 256 \times 256$ grid points. To train the 3D NNs, we generated a total of 2,000 data-label pairs, with an additional 200 data-label pairs for validation. Each image (or label) contains $N_1 \times N_2 \times N_3 = 128 \times 256 \times 256$ grid points. We also use the method described in Appendix A to generate a set of PP, PS, SP, and SS elastic images to train elastic SCF-Net. For training and validating F-Net and SCF-Net, we simply use the PP image as the input, while for elastic SCF-Net, we use all the four images as the image input.

2.3 Training and validation

Recognizing the fact that a fault label are highly unbalanced with the background (non-fault region) in terms of number of pixels, we use a hybrid loss function consisting of dice loss (Sudre et al., 2017) and L_1 losses to train SCF-Net:

$$\mathcal{L} = \lambda_1 \mathcal{L}_{\text{probability}} + \lambda_2 \mathcal{L}_{\text{dip}} + \lambda_3 \mathcal{L}_{\text{strike}}, \tag{13}$$

$$= \lambda_1 \left(1 - \frac{2\sum_{i=1}^{N} p_i g_i + \varepsilon}{\sum_{i=1}^{N} p_i + \sum_{i=1}^{N} g_i + \varepsilon}\right) + \lambda_2 \frac{1}{N} \sum_{i=1}^{N} |\theta_i - \Theta_i| + \lambda_3 \frac{1}{N} \sum_{i=1}^{N} |\phi_i - \Phi_i|, \tag{14}$$

where $\varepsilon = 1$ is a smoothing factor to avoid zero denominator, N is the total number of pixels/voxels in the image; p_i and g_i represent the NN-predicted and label fault probability, respectively; θ_i and

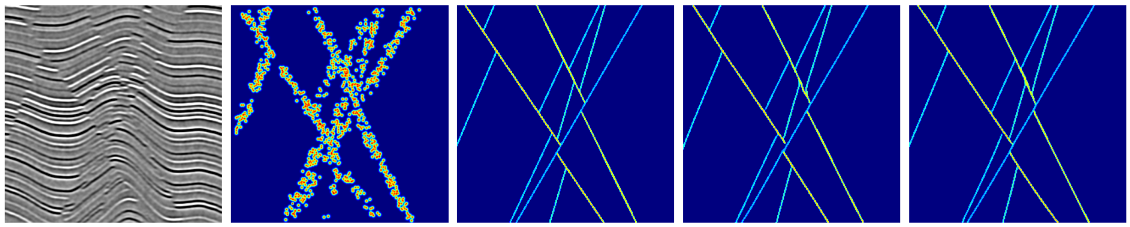

(a)

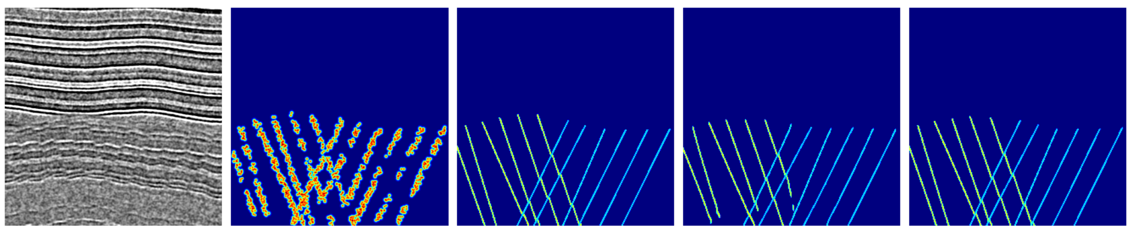

(b)

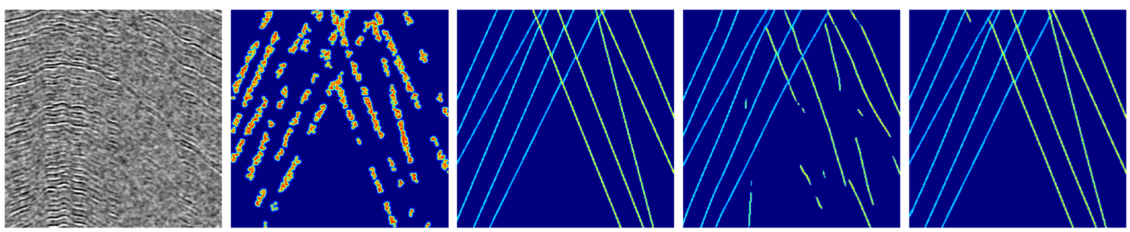

(c)

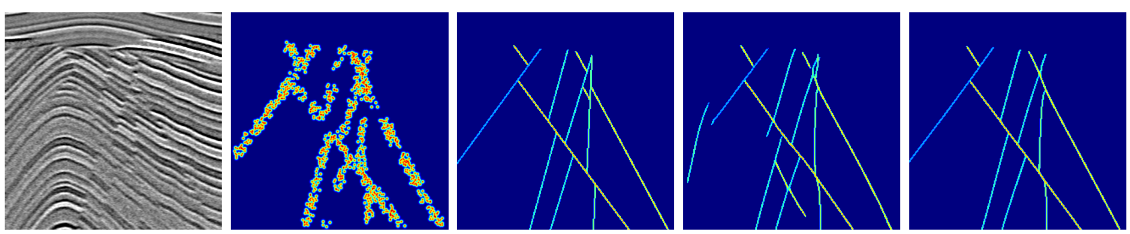

(d)

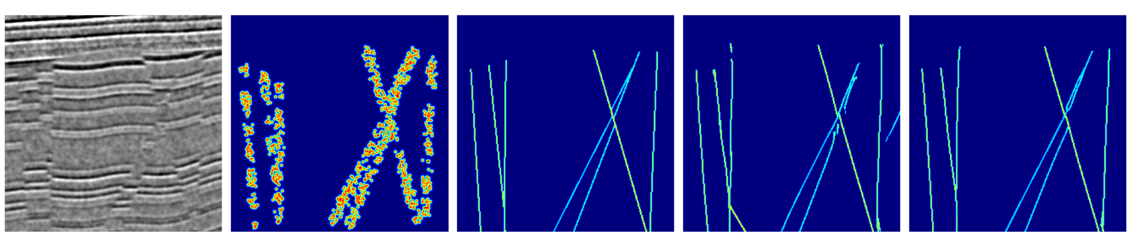

(e)

Figure 4: Panels (a-e) display five examples of synthetic seismic migration images generated by RGM and the corresponding ML inference results. For simplicity, we ignore the axis ticks and labels in these plots. Columns 1–5 represent the synthetic image, the source image, the ground-truth fault dip image, the fault dip image inferred by F-Net, and by SCF-Net, respectively. The inference output also include fault probability; here, for simplicity we do not show the probability images, but the pattern of fault probability is essentially same with fault dip (and fault strike in the 3D scenario).

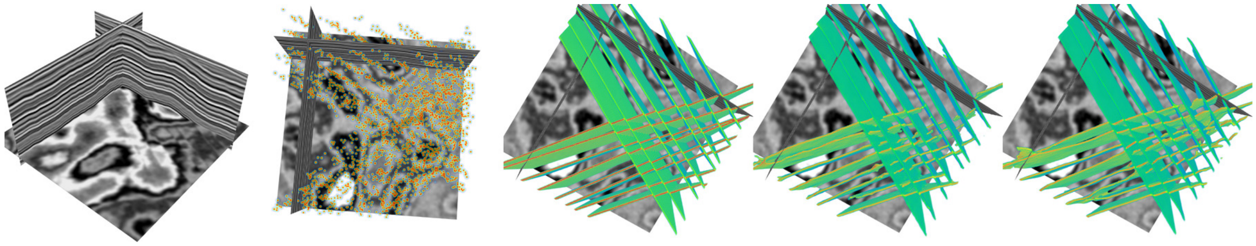

(a)

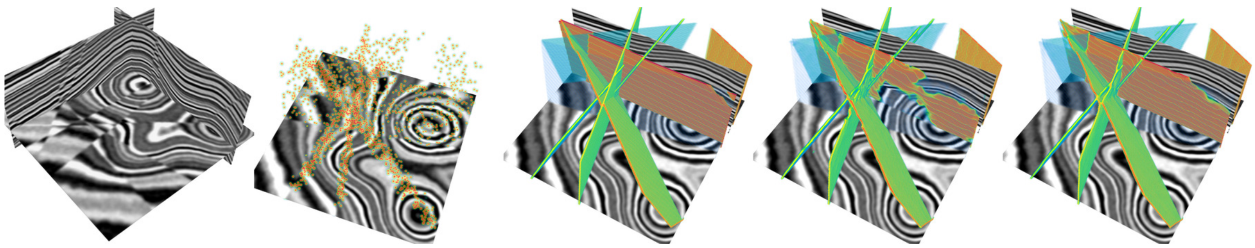

(b)

Figure 5: Panels (a-b) display two examples of synthetic 3D seismic images, labels, and ML inference. From the left to the right, the five columns represent the seismic image, the source location (as volume rendering), the ground-truth fault strike image, the fault strike inferred by F-Net, and the fault strike inferred by SCF-Net.

Θ represent the NN-predicted and label fault dips, respectively; and ϕ_i and Φ_i represent the NN-predicted and label fault strikes, respectively. The three coefficients, λ_1, λ_2, and λ_3, are weighting factors for different loss terms, where we choose $\lambda_2 = \lambda_3 = 10\lambda_1$.

We implement F-Net, SCF-Net, and elastic SCF-Net using PyTorch interfaced through PyTroch Lightning (Falcon, 2019). We train all the 2D models, including F-Net, SCF-Net, and elastic SCF-Net detailed in Appendix A, using one NVIDIA 3090 graphics processing unit (GPU) card, with a batch size of eight, and train all the 3D models with eight NVIDIA A100 GPU cards using a batch size of eight. We use an Adam optimizer (Kingma and Ba, 2017) to train the 2D and 3D versions of SCF-Net with an initial learning rate of 0.5×10^{-4}, and reduce the learning rate by ten times if there is no reduction of validation loss consecutively for 10 iterations.

We inspect the efficacy and accuracy of the trained models on the validation dataset in Figures 4 and 5 for 2D and 3D scenarios, respectively. Four of the five fault dip maps corresponding to the synthetic images (panels b to e) inferred by F-Net display an evident discrepancy between the labels and the prediction, especially on the noisy image in Figure 4c. By contrast, by effectively exploiting seismicity location information associated with the image, SCF-Net achieves an improved accuracy for all the five seismic images. We observe that SCF-Net achieves similar accuracy for other images in the validation dataset.

The comparison on two 3D synthetic images displayed in Figure 5 resembles the comparison in Figure 4. For first image, we observe that F-Net misses some subtle faults within the interlacing

Metrics	2D		3D	
	No Seismicity	**With Seismicity**	**No Seismicity**	**With Seismicity**
Fault Probability Loss	0.171	0.119	0.167	0.129
Fault Dip Loss	0.103	0.0728	0.116	0.0901
Fault Strike Loss	N/A	N/A	0.125	0.0954
Total Loss	0.274	0.191	0.408	0.314
Precision	0.837	0.882	0.839	0.872
Accuracy	0.980	0.986	0.978	0.983
Recall	0.822	0.881	0.828	0.871
SSIM	0.906	0.935	0.895	0.923

Table 1: Comparison of metrics between F-Net and SCF-Net. All the values are associated with the validation dataset that is non-overlapping with the training dataset.

fault network on the right region of the image, while for the second image, F-Net predicts an incomplete fault surface (the orange-colored one in the middle of the image). On the contrary, SCF-Net generates accurate inference of the interlacing fault network for the first image and a complete fault surface for the second image, both of which are close to the ground-truth fault surfaces in the middle column.

Table 1 displays various metrics associated with the validation datasets in the 2D and 3D scenarios. Note that some of the metrics, including precision, accuracy, recall (e.g., Wu et al., 2019a), and structural similarity index measure (SSIM) (Wang et al., 2004), are defined for the fault probability output only. For both 2D and 3D models, we observe an evident improvement in precision, accuracy, recall, and structural similarity index measure by SCF-Net compared with F-Net. These metrics are consistent with our qualitative analysis above, and demonstrate the evident advantage of image-location integration for fault detection and characterization.

3 Results

We further validate the efficacy of our SCF-Net with field seismic images. High-quality seismic migration images and source images are rare and mostly proprietary. In the following two examples, we use open-source seismic migration images generated based on marine seismic data. However, the MEQs in these two examples are not results based on field data, but are created by us based on preliminary detection of geological faults on these image using a multitask model (Gao, 2024).

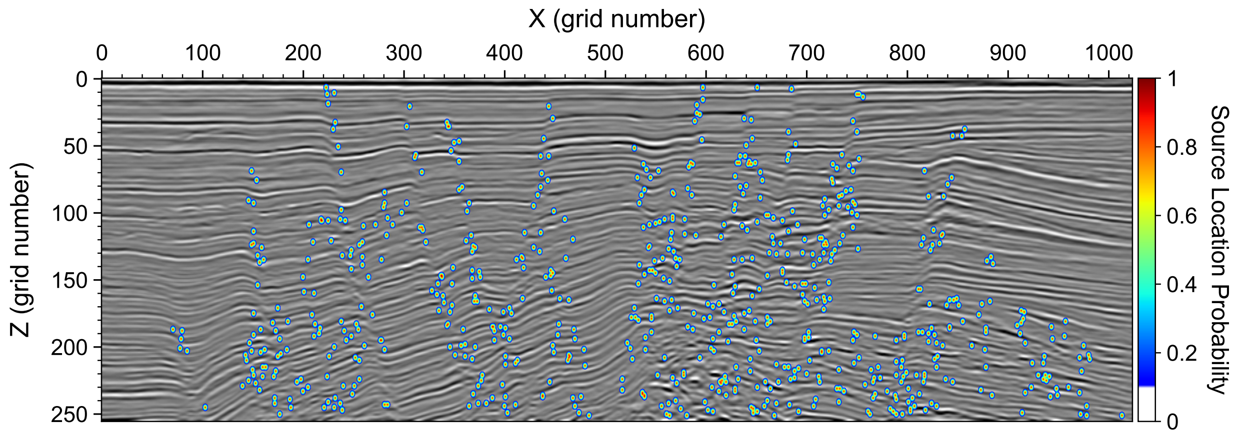

Figure 6: A 2D slice of Opunake image overlain by randomly distributed MEQs.

Nevertheless, they suffice for demonstrating the efficacy of SCF-Net.

3.1 Opunake image

The first image, displayed in Figure 6, is a 2D vertical slice from the Opunake 3D migration image volume provided by New Zealand Crown Minerals (SEG, 2020a). The image is sampled by 256 grid points in the vertical direction and 1024 grid points in the horizontal direction. Visually, there are several major and also small-scale faults developing in this image, with a particularly complex fault system that is challenging to delineate by hand in the lower-center region.

We apply F-Net and SCF-Net trained by the aforementioned synthetic data-labels to the image, and obtain fault probability and fault dip images displayed in Figure 7a and b, respectively. While both models delineate a number of major and minor faults from the image, we observe that SCF-Net outperforms F-Net by more accurately delineating more small-scale isolated or interlacing faults in the lower-center region. For instance, at the horizontal position of 550 and at the depth of 200, F-Net without seismicity constraint misses a major near-vertical fault, which, by contrast, is captured by SCF-Net. SCF-Net also captures a number of small-scale faults between the depths of 200 and 250, and between the horizontal positions of 650 and 900.

In parallel, we notice that both F-Net and SCF-Net can capture the dip angle of the faults. In particular, they can capture continuously varying dip angles of the curved faults (e.g., the three major faults on the left part of the image), even though both of them are trained with synthetic images where each of the faults has a constant dip angle. This validates the efficacy of our method of data generation and the end-to-end architecture.

We further inspect the consistency between the seismicity location and the inferred faults. Figure 8a displays the fault dip image inferred by F-Net overlying on the seismicity location represented by black dots. Since F-Net does not use seismicity location information, it is not

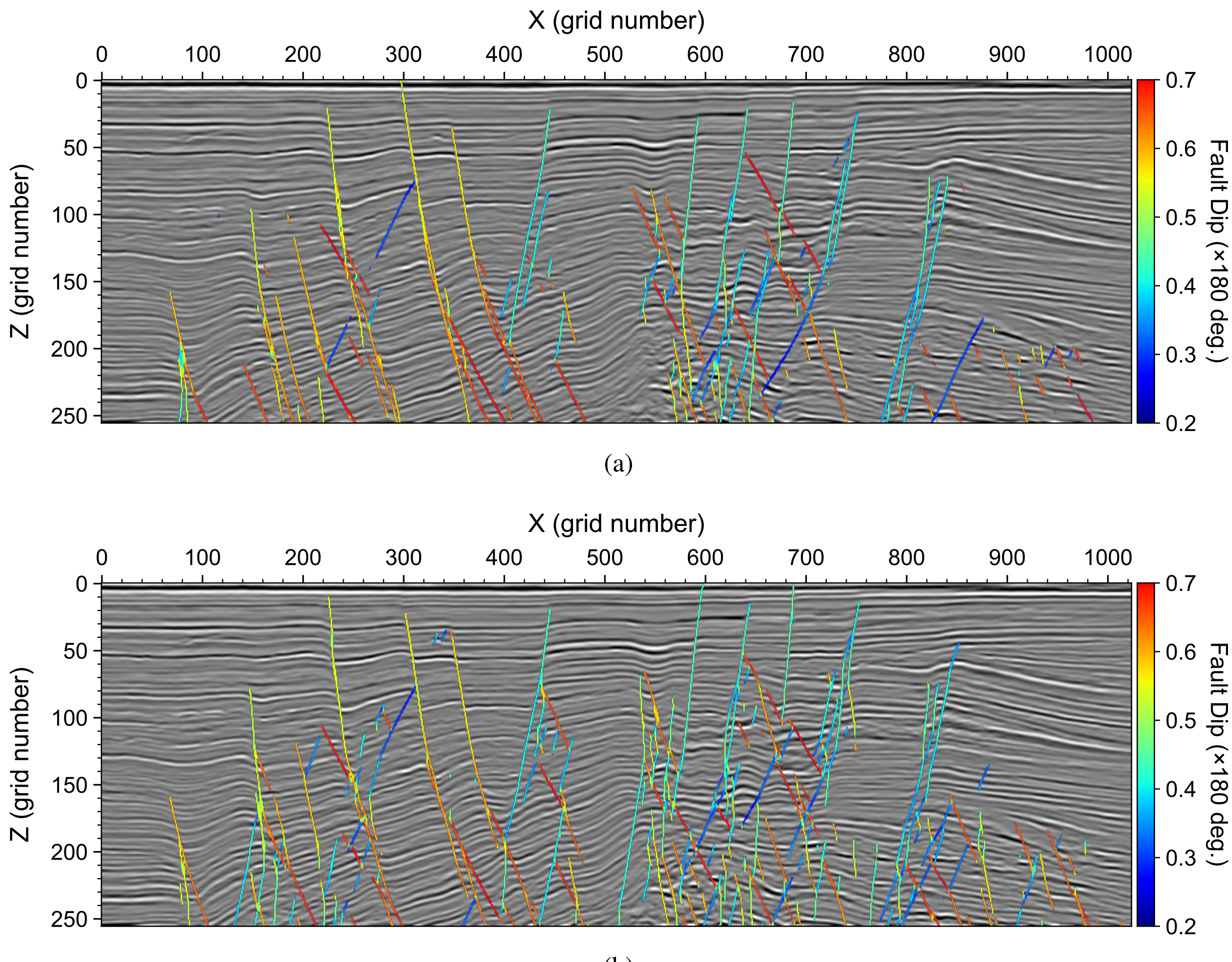

Figure 7: Fault dip inference obtained by (a) F-Net and (b) SCF-Net, both overlying on the input migration image displayed in Figure 6.

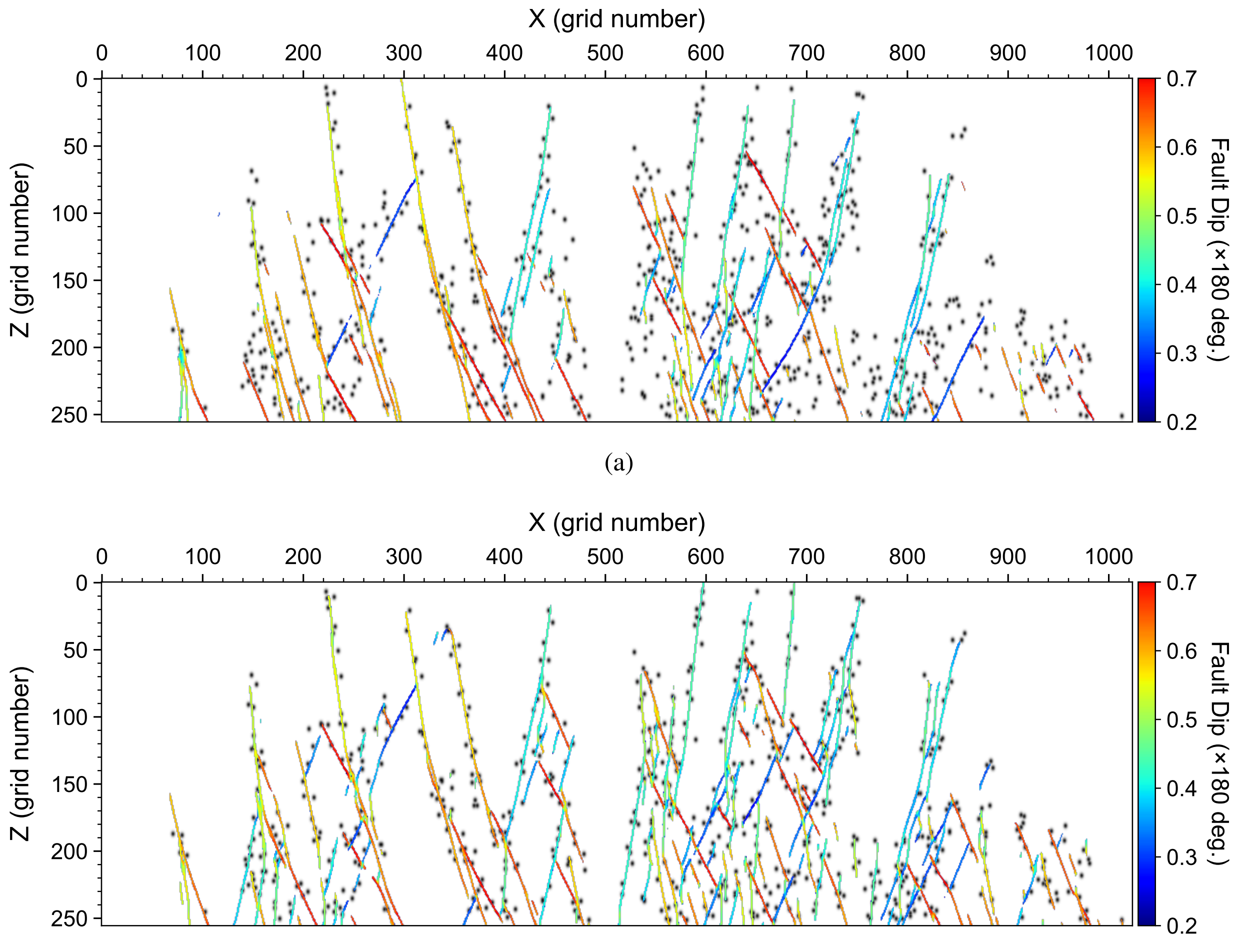

(a)

(b)

Figure 8: Fault dip inference obtained by (a) F-Net and (b) SCF-Net, both overlying on ground-truth MEQ locations.

surprising to observe that F-Net-detected faults miss numerous seismicity, particularly in the lower-right region of the image. On the contrary, the consistency between the seismicity location map and the faults inferred by SCF-Net displayed in Figure 8b attains an evident improvement, and most of, if not all of, the seismicity are correlated with some fault, even in the lower-right region. We provide a zoom-in comparison of the results obtained by F-Net and SCF-Net in Figure 9 for the lower-right region of the image, which demonstrates the improvement of fault detection when it is constrained by seismicity location.

3.2 North Sea F3 image

In the second example, we use a 3D image volume to demonstrate the efficacy and accuracy of SCF-Net.

Figure 10 displays a portion of the Project F3 seismic migration image volume, corresponding

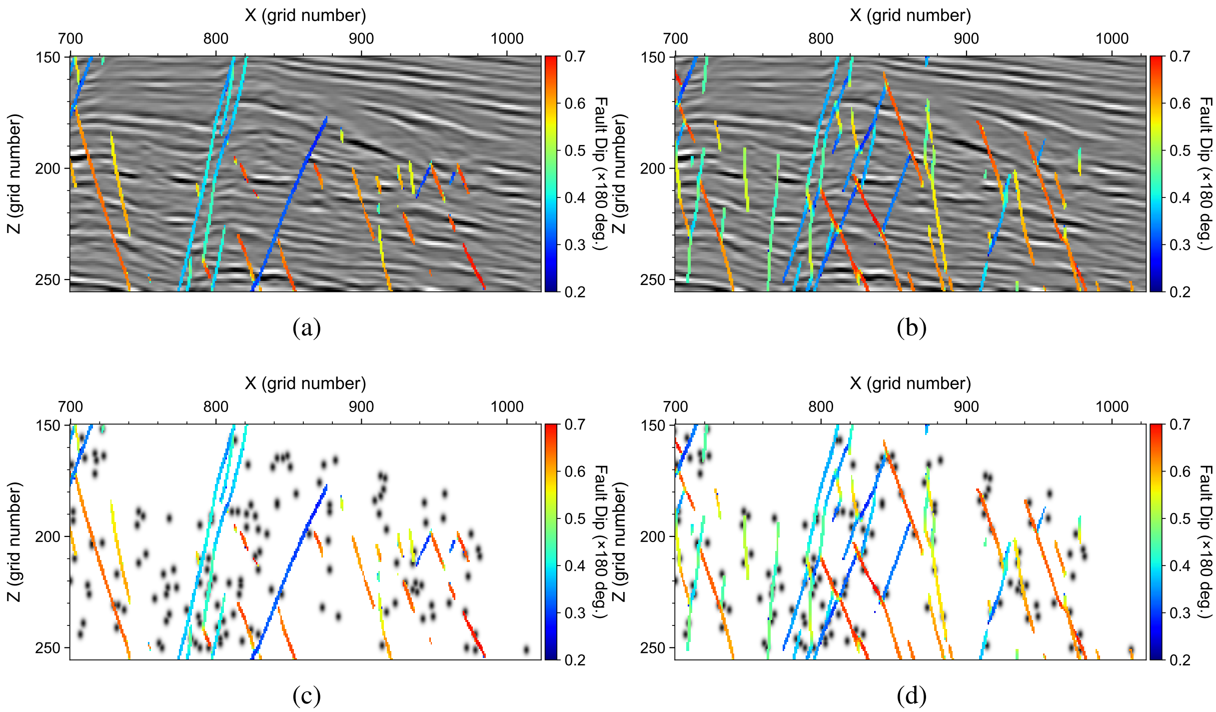

Figure 9: A zoom-in view of the results displayed in Figures 7 and 8 of fault dip inference obtained by (a, c) F-Net and (b, d) SCF-Net, overlying on the migration image and MEQ locations.

to a North Sea region in the Netherlands offshore (SEG, 2020b). The area develops rich faults, containing both quasi-parallel and intersecting faults. The selected part of the entire image contains a total of $N_1 \times N_2 \times N_3 = 128 \times 256 \times 256$ regular grid points. As in the first example, we assign a number of random seismicity based on a preliminary detection of faults from the image, and create a source image map using equation (12). The random seismicity is displayed as isolated Gaussians in Figure 10 orthogonal panels, and as green dots for better visualization in the top-right panel.

Figures 11a and b display the fault strike maps inferred by F-Net and SCF-Net, respectively. Both methods infer a number of major faults from the 3D image volume, where, based on the horizontal slice in the top-left panels of the figures, SCF-Net finds more faults, and importantly, more continuous faults. For instance, the faults detected by F-Net in the center region on the horizontal slice break into discontinuous smaller faults, while based on the detection result obtained by SCF-Net in Figure 11, it is more likely that they belong to several distinct major quasi-parallel faults. In addition, F-Net misses several evident faults in the lower-center and top-right regions on the horizontal slice, which by contrast are captured by SCF-Net. We also observe that on the $Z - Y$ vertical slice image, SCF-Net captures a set of quasi-parallel faults with high dip angles. By contrast, F-Net fails to capture some of these faults, or the captured faults are broken or incomplete, resulting in an inconsistency between the faults and the migration image. The comparison between

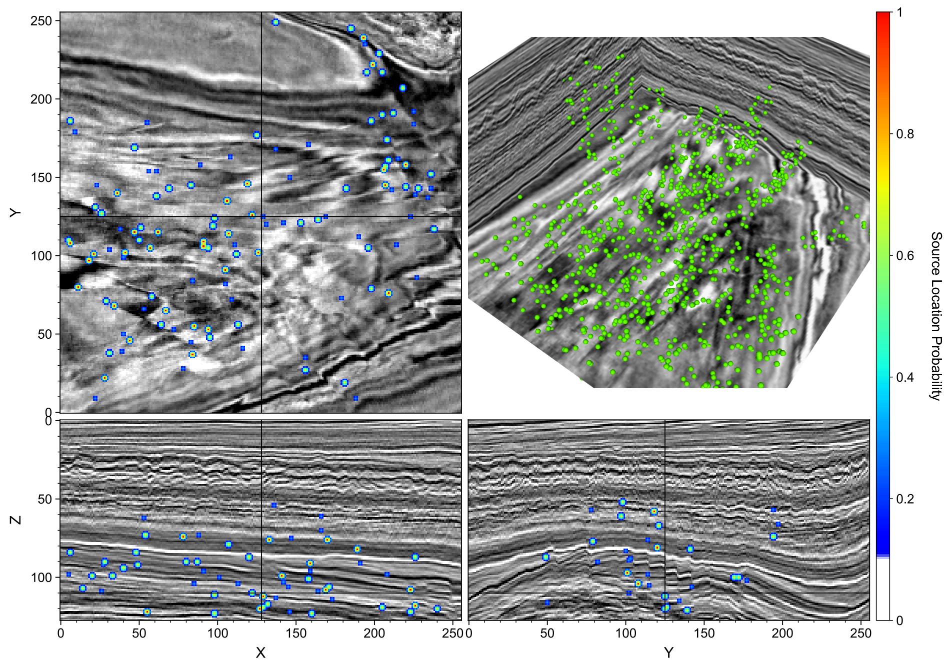

Figure 10: Fault dip inference obtained by (a) F-Net and (b) SCF-Net, both overlying on ground-truth MEQ locations.

the fault dip maps output by the two models displayed in Figure 12 resembles the comparison on fault strike maps.

We overlay the inferred fault dip maps by F-Net and SCF-Net on the seismic location map in Figures 13a and b, respectively. Compared with SCF-Net, F-Net misses two major faults that trend approximately $135° - 305°$ at $(X, Y) = (200, 220)$ and $(170, 25)$, as well as several small-scale faults that trend approximately $30° - 210°$ at $(X, Y) = (60, 25)$. These faults only have limited fault displacements, and therefore are challenging to be detected by F-Net based solely on the migration image. On the top-right panels of the two figures, we display the volume rendering of the faults inferred by the two methods along with the location of seismicity. It is evident that SCF-Net accurately recognizes the two faults missed by F-Net, resulting in an improved spatial correlation between the faults and the seismicity location.

4 Discussion

The validations based on synthetic images and field-data images demonstrated that the integration of seismicity location information with seismic migration image can notably improve the accuracy and fidelity of ML-based fault detection and characterization. However, we must remark that a seismic migration image and seismicity location image are not always both available for an area. In particular, high-resolution seismic images are mostly derived based on active-source seismic

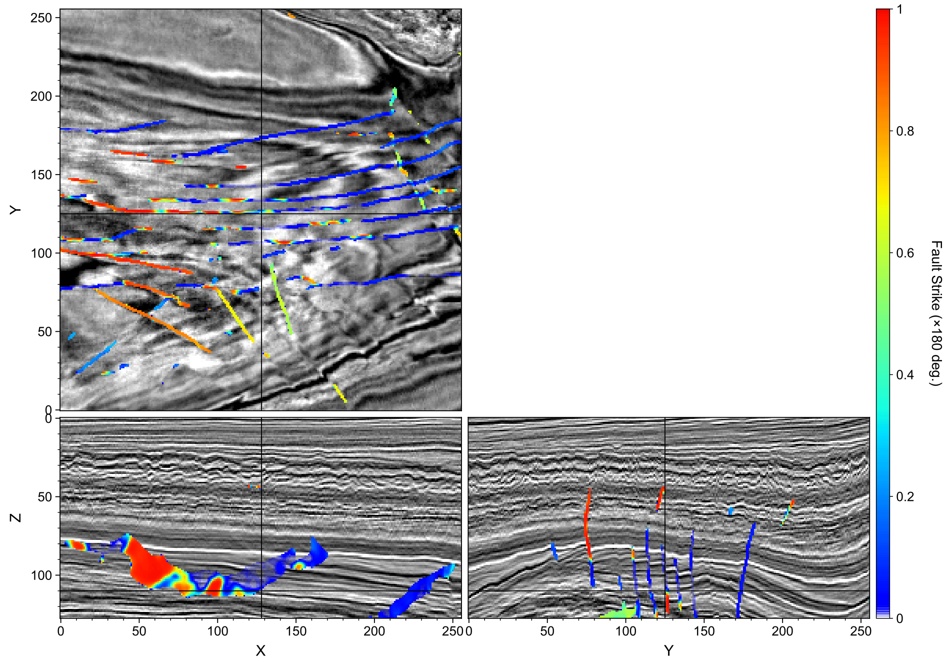

(a)

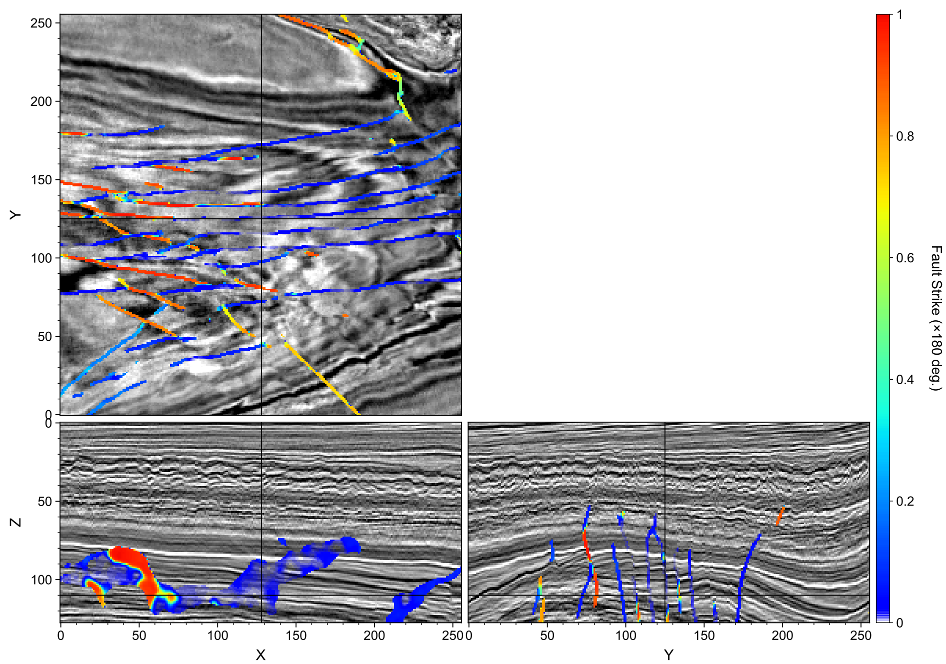

(b)

Figure 11: Fault dip inference obtained by (a) F-Net and (b) SCF-Net, both overlying on the seismic migration image.

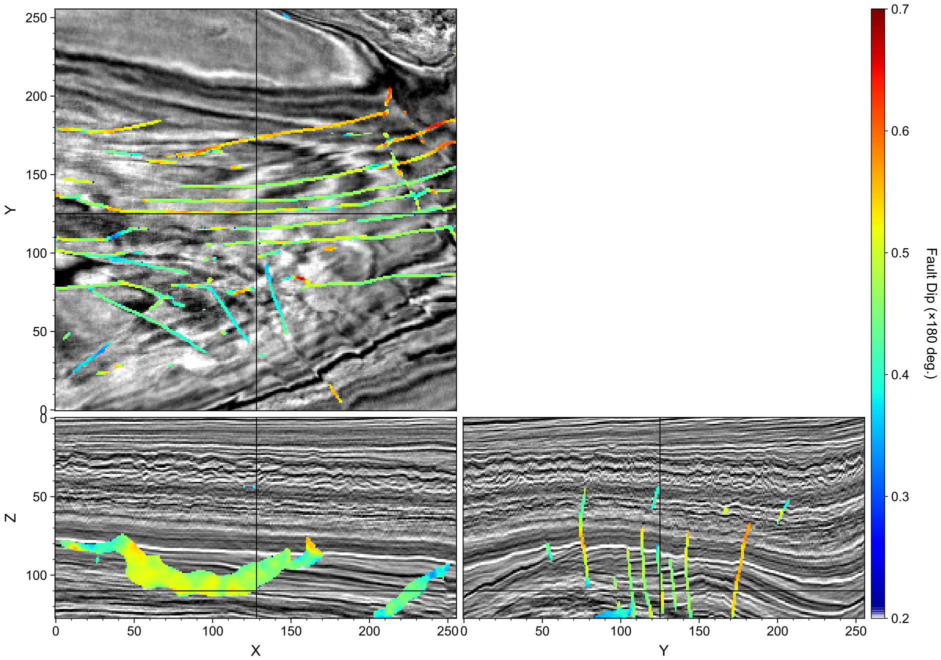

(a)

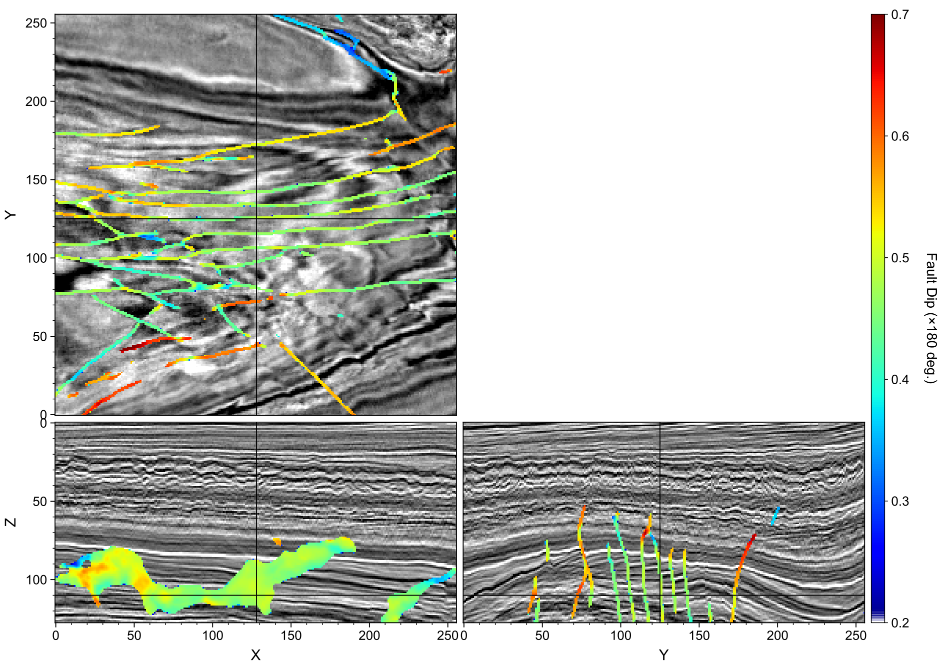

(b)

Figure 12: Fault dip inference obtained by (a) F-Net and (b) SCF-Net, both overlying on the seismic migration image.

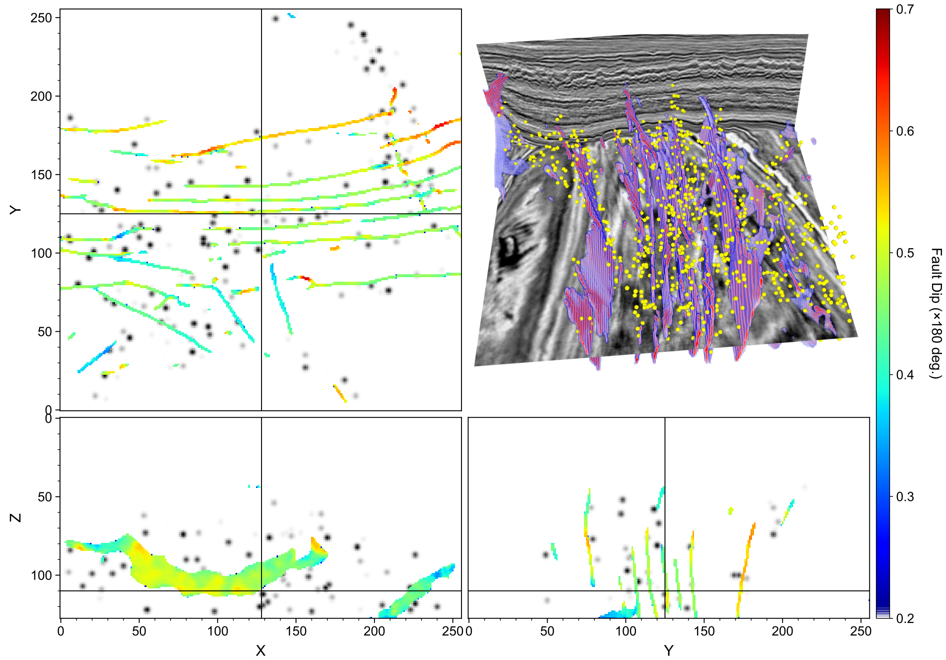

(a)

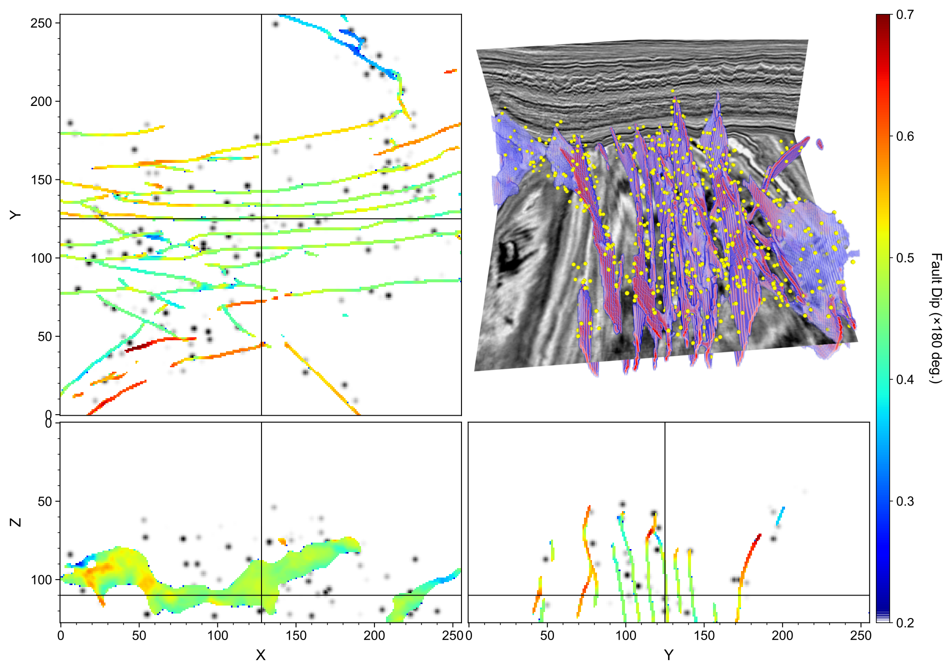

(b)

Figure 13: Fault dip inference obtained by (a) F-Net and (b) SCF-Net, both overlying on the source image.

survey data, which can be expensive to acquire and process. A high-quality seismic catalog is also necessary to ensure that observed seismic events are properly located to or near their spatial location using either traveltime or waveforms. Coherent deviation of seismicity location with respect to their true location may lead to biased fault detection results, as our ML model does not have an intrinsic mechanism to mitigate such coherent deviation (or location "noise").

The architecture we adopted to build SCF-Net is one of the many possibilities to achieve the seismicity-constrained multitask fault characterization, as is in the case of image-only fault detection paradigm. Alternative ML models, including many ViT-based and CNN-based models (e.g., Bi et al., 2021; Wang et al., 2024b), may possibly improve what we have achieved in this work after some appropriate adaption to include seismicity location. Meanwhile, the iterative refinement strategy (Gao, 2024) may also improve the fidelity and accuracy of SCF-Net. Exploration of these methods, however, is beyond the scope of this work.

5 Conclusions

We developed a supervised machine learning model to automatically identify and characterize geological faults based on both seismic image and seismicity location information. We encoded the image and seismicity via two independent encoders, and merged and decoded the learned feature maps from the two encoder branches using a unified decoder branch. To improve the receptive field of the neural network, we used small-scale residual U-Nets with large dilation ratios as the fundamental units in both the encoders and decoders. We designed subdecoders to simultaneously learn fault probability, fault dip, and fault strike maps, resulting in an end-to-end, multitask neural network. We detailed the methods and algorithms for generating high-quality seismic images, fault labels, and source images, and the strategy for training and validating the neural networks. Specially, we detailed the method for generating synthetic elastic images and a neural network architecture for detecting faults from a set of elastic migration images that contains PP, PS, SP, and SS reflectivity images. Using both synthetic and field seismic migration images, we demonstrated the efficacy and accuracy of the seismicity-constrained fault detection neural network. The results demonstrated that by integrating seismicity information to the neural network, we can notably improve the accuracy and fidelity of automatic end-to-end fault delineation and characterization. The method could serve as a powerful and high-fidelity tool for characterizing complex fault networks from seismic image and source location.

Acknowledgments

The work was supported by Los Alamos National Laboratory (LANL) Laboratory Directory Research and Development (LDRD) project 20240322ER. LANL is managed and operated by Triad National Security, LLC for the U.S. Department of Energy (DOE) National Nuclear Security Administration (NNSA) under contract No. 89233218CNA000001. The research used high-performance computing resources provided by LANL's Institutional Computing (IC) program. The paper was approved for public release under LA-UR-24-30317.

Data Availability

The codes for implementing, training, validating, and testing the ML models developed and compared in this work are open-source available at `github.com/lanl/scf`. The codes for generating the random faulted models mentioned in this paper, including the images, the fault labels, and the random source images, are open-source at the same repository for reproducibility purpose as well. The data generation is based on our Random Geological Model package (RGM) that is open-source available at `github.com/lanl/rgm` and our generic Fortran library (FLIT) that is open-source available at `github.com/lanl/flit`.

References

Aki, K., 1972, Earthquake mechanism: Tectonophysics, **13**, no. 1, 423–446, doi: 10.1016/0040-1951(72)90032-7.

Aki, K., and P. G. Richards, 2002, Quantitative Seismology: University Science Books, Sausalito, California.

An, Y., H. Du, S. Ma, Y. Niu, D. Liu, J. Wang, Y. Du, C. Childs, J. Walsh, and R. Dong, 2023, Current state and future directions for deep learning based automatic seismic fault interpretation: A systematic review: Earth-Science Reviews, **243**, 104509, doi: 10.1016/j.earscirev.2023.104509.

An, Y., J. Guo, Q. Ye, C. Childs, J. Walsh, and R. Dong, 2021, Deep convolutional neural network for automatic fault recognition from 3D seismic datasets: Computers & Geosciences, **153**, 104776, doi: 10.1016/j.cageo.2021.104776.

Bi, Z., X. Wu, Z. Geng, and H. Li, 2021, Deep relative geologic time: A deep learning method for simultaneously interpreting 3-D seismic horizons and faults: Journal of Geophysical Research: Solid Earth, **126**, no. 9, 10.1029/2021JB021882, doi: 10.1029/2021JB021882.

Chang, K. W., and P. Segall, 2016, Injection-induced seismicity on basement faults including poroelastic stressing: Journal of Geophysical Research: Solid Earth, **121**, no. 4, 2708–2726, doi: 10.1002/2015JB012561.

Chen, B., Y. Liu, Z. Zhang, G. Lu, and A. W. K. Kong, 2024, TransAttUnet: Multi-level attention-guided U-Net with transformer for medical image segmentation: IEEE Transactions on Emerging Topics in Computational Intelligence, **8**, no. 1, 55–68, doi: 10.1109/TETCI.2023.3309626.

Chen, T., and L. Huang, 2015, Directly imaging steeply-dipping fault zones in geothermal fields with multicomponent seismic data: Geothermics, **57**, 238–245, doi: https://doi.org/10.1016/j.geothermics.2015.07.003.

Chi, B., K. Gao, and L. Huang, 2021, Vector elastic deconvolution migration with dual wavefield decomposition: Geophysics, **86**, no. 4, S271–S282, doi: 10.1190/geo2020-0826.1.

Cohen, I., N. Coult, and A. A. Vassiliou, 2006, Detection and extraction of fault surfaces in 3D seismic data: Geophysics, **71**, no. 4, P21–P27, doi: 10.1190/1.2215357.

Cunha, A., A. Pochet, H. Lopes, and M. Gattass, 2020, Seismic fault detection in real data using transfer learning from a convolutional neural network pre-trained with synthetic seismic data: Computers & Geosciences, **135**, 104344, doi: 10.1016/j.cageo.2019.104344.

Di, H., M. Shafiq, and G. AlRegib, 2018, Patch-level MLP classification for improved fault detection: SEG Technical Program Expanded Abstracts, 2211–2215, doi: 10.1190/segam2018-2996921.1.

Dichiarante, A., N. Langet, R. Bauer, B. Goertz-Allmann, S. Williams-Stroud, D. Kühn, V. Oye, S. Greenberg, and B. Dando, 2021, Identifying geological structures through microseismic cluster and burst analyses complementing active seismic interpretation: Tectonophysics, **820**, 229107, doi: 10.1016/j.tecto.2021.229107.

Dosovitskiy, A., L. Beyer, A. Kolesnikov, D. Weissenborn, X. Zhai, T. Unterthiner, M. Dehghani, M. Minderer, G. Heigold, S. Gelly, J. Uszkoreit, and N. Houlsby, 2021, An image is worth 16 × 16 words: Transformers for image recognition at scale: International Conference on Learning Representations (ICLR), doi: openreview.net/forum?id=YicbFdNTTy.

Ellsworth, W. L., 2013, Injection-induced earthquakes: Science, **341**, no. 6142, 1225942, doi: 10.1126/science.1225942.

Falcon, W., 2019, Pytorch lightning: GitHub, **3**, doi: github.com/PyTorchLightning/pytorch-lightning.

Gao, K., 2024, Iterative multitask learning and inference from seismic images: Geophysical Journal International, **236**, no. 1, 565–592, doi: 10.1093/gji/ggad424.

Gao, K., and T. Chen, 2024, Random geological model generation package: GitHub Repository, doi: github.com/lanl/rgm.

Gao, K., L. Huang, and T. Cladouhos, 2021, Three-dimensional seismic characterization and imaging of the Soda Lake geothermal field: Geothermics, **90**, 101996, doi: 10.1016/j.geothermics.2020.101996.

Gao, K., L. Huang, and Y. Zheng, 2022a, Fault detection on seismic structural images using a nested residual U-Net: IEEE Transactions on Geoscience and Remote Sensing, **60**, 1–15, doi: 10.1109/tgrs.2021.3073840.

Gao, K., L. Huang, Y. Zheng, R. Lin, H. Hu, and T. Cladohous, 2022b, Automatic fault detection on seismic images using a multiscale attention convolutional neural network: Geophysics, **87**, no. 1, N13–N29, doi: 10.1190/geo2020-0945.1.

Glubokovskikh, S., E. Saygin, S. Shapiro, B. Gurevich, R. Isaenkov, D. Lumley, R. Nakata, J. Drew, and R. Pevzner, 2022, A small CO_2 leakage may induce seismicity on a sub-seismic fault in a good-porosity clastic saline aquifer: Geophysical Research Letters, **49**, no. 12, e2022GL098062, doi: 10.1029/2022GL098062.

Hale, D., 2013, Methods to compute fault images, extract fault surfaces, and estimate fault throws from 3D seismic images: Geophysics, **78**, no. 2, O33–O43, doi: 10.1190/geo2012-0331.1.

Kingma, D. P., and J. Ba, 2017, Adam: A method for stochastic optimization: International Conference on Learning Representations (ICLR), doi: dare.uva.nl/search?identifier=a20791d3-1aff-464a-8544-268383c33a75.

LeCun, Y., L. Bottou, Y. Bengio, and P. Haffner, 1998, Gradient-based learning applied to document recognition: Proceedings of the IEEE, **86**, no. 11, 2278–2324, doi: 10.1109/5.726791.

Li, L., J. Tan, B. Schwarz, F. Staněk, N. Poiata, P. Shi, L. Diekmann, L. Eisner, and D. Gajewski, 2020, Recent advances and challenges of waveform-based seismic location methods at multiple scales: Reviews of Geophysics, **58**, no. 1, e2019RG000667, doi: 10.1029/2019RG000667. (e2019RG000667 2019RG000667).

Liu, Z., Y. Lin, Y. Cao, H. Hu, Y. Wei, Z. Zhang, S. Lin, and B. Guo, 2021, Swin transformer: Hierarchical vision transformer using shifted windows: IEEE/CVF International Conference on Computer Vision (ICCV), 9992–10002, doi: 10.1109/ICCV48922.2021.00986.

Manzocchi, T., C. C., and J. J. Walsh, 2010, Faults and fault properties in hydrocarbon flow models: Geofluids, **10**, no. 1-2, 94–113, doi: 10.1111/j.1468-8123.2010.00283.x.

Marfurt, K. J., R. L. Kirlin, S. L. Farmer, and M. S. Bahorich, 1998, 3-D seismic attributes using a semblance-based coherency algorithm: Geophysics, **63**, no. 4, 1150–1165, doi: 10.1190/1.1444415.

Marfurt, K. J., V. Sudhaker, A. Gersztenkorn, K. D. Crawford, and S. E. Nissen, 1999, Coherency calculations in the presence of structural dip: Geophysics, **64**, no. 1, 104–111, doi: 10.1190/1.1444508.

Murphy, K. P., 2022, Probabilistic machine learning: An introduction: MIT Press.

Nakata, N., and G. C. Beroza, 2016, Reverse time migration for microseismic sources using the geometric mean as an imaging condition: Geophysics, **81**, no. 2, KS51–KS60, doi: 10.1190/geo2015-0278.1.

Park, Y., G. C. Beroza, and W. L. Ellsworth, 2022, Basement fault activation before larger earthquakes in Oklahoma and Kansas: The Seismic Record, **2**, no. 3, 197–206, doi: 10.1785/0320220020.

Paszke, A., S. Gross, F. Massa, A. Lerer, J. Bradbury, G. Chanan, T. Killeen, Z. Lin, N. Gimelshein, L. Antiga, A. Desmaison, A. Kopf, E. Yang, Z. DeVito, M. Raison, A. Tejani, S. Chilamkurthy, B. Steiner, L. Fang, J. Bai, and S. Chintala, 2019, Pytorch: An imperative style, high-performance deep learning library, *in* Advances in Neural Information Processing Systems 32: Curran Associates, Inc., 8024–8035.

Pedersen, S., T. Randen, L. Sonneland, and O. Steen, 2002, Automatic 3d fault interpretation by artificial ants: Extended Abstracts of 64th European Association of Geoscientists & Engineers Conference & Exhibition, doi: 10.3997/2214-4609-pdb.5.G037.

Qin, X., Z. Zhang, C. Huang, M. Dehghan, O. R. Zaiane, and M. Jagersand, 2020, U^2-Net: Going deeper with nested U-structure for salient object detection: Pattern Recognition, **106**, 107404, doi: 10.1016/j.patcog.2020.107404.

Rodriguez, M. Z., C. H. Comin, D. Casanova, O. M. Bruno, D. R. Amancio, L. d. F. Costa, and F. A. Rodrigues, 2019, Clustering algorithms: A comparative approach: PLoS One, **14**, no. 1, e0210236, doi: 10.1371/journal.pone.0210236.

Ronneberger, O., P. Fischer, and T. Brox, 2015, U-Net: Convolutional networks for biomedical image segmentation: Proceedings of Medical Image Computing and Computer-Assisted Intervention, 234–241.

Schuster, G. T., J. Yu, J. Sheng, and J. Rickett, 2004, Interferometric/daylight seismic imaging: Geophysical Journal International, **157**, no. 2, 838–852, doi: 10.1111/j.1365-246X.2004.02251.x.

SEG, 2020a, New Zealand Opunake 3D data: SEG Wiki, wiki.seg.org/wiki/Opunake-3D.

———, 2020b, The Netherlands North Sea F3 3D data: SEG Wiki, wiki.seg.org/wiki/F3_Netherlands.

Sudre, C. H., W. Li, T. Vercauteren, S. Ourselin, and M. Jorge Cardoso, 2017, Generalised dice overlap as a deep learning loss function for highly unbalanced segmentations: Deep Learning in Medical Image Analysis and Multimodal Learning for Clinical Decision Support, 240–248, doi: 10.1007/978-3-319-67558-9_28.

Ulyanov, D., A. Vedaldi, and V. S. Lempitsky, 2016, Instance normalization: The missing ingredient for fast stylization: arXiv preprint, arxiv.org/abs/1607.08022.

Vaswani, A., N. Shazeer, N. Parmar, J. Uszkoreit, L. Jones, A. N. Gomez, L. u. Kaiser, and I. Polosukhin, 2017, Attention is all you need: Advances in Neural Information Processing Systems, **30**, doi: proceedings.neurips.cc/paper_files/paper/2017/file/3f5ee243547dee91fbd053c1c4a845aa-Paper.pdf.

Waldhauser, F., and W. L. Ellsworth, 2000, A double-difference earthquake location algorithm: Method and application to the Northern Hayward Fault, California: Bulletin of the Seismological Society of America, **90**, no. 6, 1353–1368, doi: 10.1785/0120000006.

Wang, J., S. Ma, Y. An, and R. Dong, 2024a, A comparative study of vision transformer and convolutional neural network models in geological fault detection: IEEE Access, 1–1, doi: 10.1109/ACCESS.2024.3433612.

Wang, S., X. Si, Z. Cai, L. Sun, W. Wang, and Z. Jiang, 2024b, Fast global self-attention for seismic image fault identification: IEEE Transactions on Geoscience and Remote Sensing, **62**, 1–11, doi: 10.1109/TGRS.2024.3436066.

Wang, Z., A. Bovik, H. Sheikh, and E. Simoncelli, 2004, Image quality assessment: from error visibility to structural similarity: IEEE Transactions on Image Processing, **13**, no. 4, 600–612, doi: 10.1109/TIP.2003.819861.

Wu, W., Y. Yang, B. Wu, D. Ma, Z. Tang, and X. Yin, 2023, MTL-FaultNet: Seismic data reconstruction assisted multitask deep learning 3-D fault interpretation: IEEE Transactions on Geoscience and Remote Sensing, **61**, 1–15, doi: 10.1109/TGRS.2023.3299378.

Wu, X., 2017, Directional structure-tensor-based coherence to detect seismic faults and channels: Geophysics, **82**, no. 2, A13–A17, doi: 10.1190/geo2016-0473.1.

Wu, X., and S. Fomel, 2018, Automatic fault interpretation with optimal surface voting: Geophysics, **83**, no. 5, O67–O82, doi: 10.1190/geo2018-0115.1.

Wu, X., and Z. Guo, 2018, Detecting faults and channels while enhancing seismic structural and stratigraphic features: Interpretation, **7**, no. 1, T155–T166, doi: 10.1190/INT-2017-0174.1.

Wu, X., L. Liang, Y. Shi, and S. Fomel, 2019a, FaultSeg3D: Using synthetic data sets to train an end-to-end convolutional neural network for 3D seismic fault segmentation: Geophysics, **84**, no. 3, IM35–IM45, doi: 10.1190/geo2018-0646.1.

Wu, X., L. Liang, Y. Shi, Z. Geng, and S. Fomel, 2019b, Multitask learning for local seismic image processing: fault detection, structure-oriented smoothing with edge-preserving, and seismic normal estimation by using a single convolutional neural network: Geophysical Journal International, **219**, no. 3, 2097–2109, doi: 10.1093/gji/ggz418.

Wu, X., Y. Shi, S. Fomel, L. Liang, Q. Zhang, and A. Z. Yusifov, 2019c, FaultNet3D: Predicting fault probabilities, strikes, and dips with a single convolutional neural network: IEEE Transactions on Geoscience and Remote Sensing, **57**, no. 11, 9138–9155, doi: 10.1109/tgrs.2019.2925003.

Xiong, W., X. Ji, Y. Ma, Y. Wang, N. M. AlBinHassan, M. N. Ali, and Y. Luo, 2018, Seismic fault detection with convolutional neural network: Geophysics, **83**, no. 5, O97–O103, doi: 10.1190/geo2017-0666.1.

Yang, J., X. Wu, Z. Bi, and Z. Geng, 2023, A multi-task learning method for relative geologic time, horizons, and faults with prior information and transformer: IEEE Transactions on Geoscience and Remote Sensing, **61**, 1–20, doi: 10.1109/TGRS.2023.3264593.

Appendix A: Multitask fault detection and characterization on elastic images constrained by seismicity

Our SCF-Net also applies to elastic migration images and seismicity map. In practice, elastic migration generates a set of elastic reflectivity images rather than merely a PP image (Chen and Huang, 2015; Chi et al., 2021). Therefore, for elastic SCF-Net, the input seismic image contains four images: PP, PS, SP, and SS images. Depending on the type of the source in elastic migration (explosion, vertical force vector, shear, and so on), not all the four elastic images are available or of the same quality. Here, we demonstrate the efficacy of our SCF-Net using seismicity location map and all the four elastic images, but elastic SCF-Net can be straightforwardly modified to use some of the elastic images (e.g., PP and PS images, or SP and SS images).

Although for the acoustic imaging scenario we can create a synthetic migration image by convolving a random, sparse, delta-width reflectivity image with a band-limited source wavelet, for elastic scenario, the generation of images becomes much more complex because of several factors. Firstly, different from acoustic reflectivity, elastic reflectivity contains PP, PS, SP, and SS reflectivity. The signs and magnitude of the four quantities for a same reflector are essentially different. Secondly, in elastic migration, the resolution of the PP, PS, SP, SS images are different. For some source wavelet, the resolution γ of the images generally follows $\gamma_{pp} < \gamma_{ps} = \gamma_{sp} < \gamma_{ss}$. This is because the spatial wavelength of S-wave is higher than that of the P-wave. If one generates elastic images without considering these two factors, the fidelity of the generated elastic images can be low and generally cannot resemble the amplitude (reflectivity) and resolution (wavelength) characteristics of realistic elastic migration.

To improve the fidelity of synthetic elastic images, we use theoretical elastic reflection coefficients in the generation procedure. For an interface that separates two elastic media $(\alpha_1, \beta_1, \rho_1)$ and

$(\alpha_2, \beta_2, \rho_2)$, the theoretical elastic reflection coefficients read (Aki and Richards, 2002):

$$R_{pp} = \left[\left(b\frac{\cos i_1}{\alpha_1} - c\frac{\cos i_2}{\alpha_2} \right) F - \left(a + d\frac{\cos i_1}{\alpha_1}\frac{\cos j_2}{\beta_2} \right) Hp^2 \right] D^{-1}, \tag{15}$$

$$R_{ps} = -2\frac{\cos i_1}{\alpha_1} \left(ab + cd\frac{\cos i_2}{\alpha_2}\frac{\cos j_2}{\beta_2} \right) p\alpha_1 (\beta_1 D)^{-1}, \tag{16}$$

$$R_{sp} = -2\frac{\cos j_1}{\beta_1} \left(ab + cd\frac{\cos i_2}{\alpha_2}\frac{\cos j_2}{\beta_2} \right) p\beta_1 (\alpha_1 D)^{-1}, \tag{17}$$

$$R_{ss} = \left[\left(b\frac{\cos j_1}{\beta_1} - c\frac{\cos j_2}{\beta_2} \right) E - \left(a + d\frac{\cos i_2}{\alpha_2}\frac{\cos j_1}{\beta_1} \right) Gp^2 \right] D^{-1}, \tag{18}$$

where

$$E = b\frac{\cos i_1}{\alpha_1} + c\frac{\cos i_2}{\alpha_2}, \tag{19}$$

$$F = b\frac{\cos j_1}{\beta_1} + c\frac{\cos j_2}{\beta_2}, \tag{20}$$

$$G = a - d\frac{\cos i_1}{\alpha_1}\frac{\cos j_2}{\beta_2}, \tag{21}$$

$$H = a - d\frac{\cos i_2}{\alpha_2}\frac{\cos j_1}{\beta_1}, \tag{22}$$

$$D = EF + GHp^2, \tag{23}$$

$$a = \rho_2(1 - 2\beta_2^2 p^2) - \rho_1(1 - 2\beta_1^2 p^2), \tag{24}$$

$$b = \rho_2(1 - 2\beta_2^2 p^2) + 2\rho_1\beta_1^2 p^2, \tag{25}$$

$$c = \rho_1(1 - 2\beta_1^2 p^2) + 2\rho_2\beta_2^2 p^2, \tag{26}$$

$$d = 2(\rho_2\beta_2^2 - \rho_1\beta_1^2), \tag{27}$$

and

$$p = \frac{\sin i_1}{\alpha_1} = \frac{\sin i_2}{\alpha_2} = \frac{\sin j_1}{\beta_1} = \frac{\sin j_2}{\beta_2} \tag{28}$$

is the ray parameter. For an incidence angle i_1, the other three incidence or transmission angles (j_1, i_2 and j_2) could be computed using the ray parameter equation straightforwardly.

Reflection coefficients are dependent on ray parameter (or equivalently, incident angle i_1 and j_1). Hence, in a rigorous setting, seismic migration images are angle-dependent prior to stack. In this work, we focus on inferring fault attributes from poststack seismic images. It is not difficult to compute and know that for an incident P-wave, $R_{ps} = 0$ when $i_1 = 0$. Similarly, for an incident S-wave, $R_{sp} = 0$ when $j_1 = 0$. Therefore, to properly synthesize elastic migration images and avoid annihilating elastic reflection coefficients, we sum the elastic coefficients from $i_1 \in [0°, 15°]$ with an interval of 3°, and use the averaged summation as the effective elastic reflection coefficients. The

Metrics	**2D**	**3D**
Fault Probability Loss	0.116	0.131
Fault Dip Loss	0.0705	0.0919
Fault Strike Loss	N/A	0.0959
Total Loss	0.186	0.319
Precision	0.889	0.866
Accuracy	0.986	0.983
Recall	0.88	0.872
SSIM	0.936	0.921

Table 2: Metrics of SCF-Net trained on seismicity and elastic migration images. All the metrics are associated with the validation dataset.

strategy is not necessarily the optimal approach to approximating the true amplitude characteristics of realistic elastic migration images, but can serve as a reasonable approach to mimicking the relative amplitude characteristics of elastic migration images, which is sufficient for a neural network to learn and infer faults.

Based on the metrics displayed in Table 2, we find that SCF-Net trained on elastic images does not essentially differ from SCF-Net trained on acoustic images in terms of loss, precision, accuracy, recall score, or SSIM, although subtle differences exist. Nevertheless, elastic SCF-Net provides a first-of-its-kind systematic approach to detecting and characterizing geological faults directly on elastic migration images that include PP, PS, SP, and SS images. Our future work may focus on improving its performance by designing more flexible architecture that can more effectively exploit information embedded in elastic images.

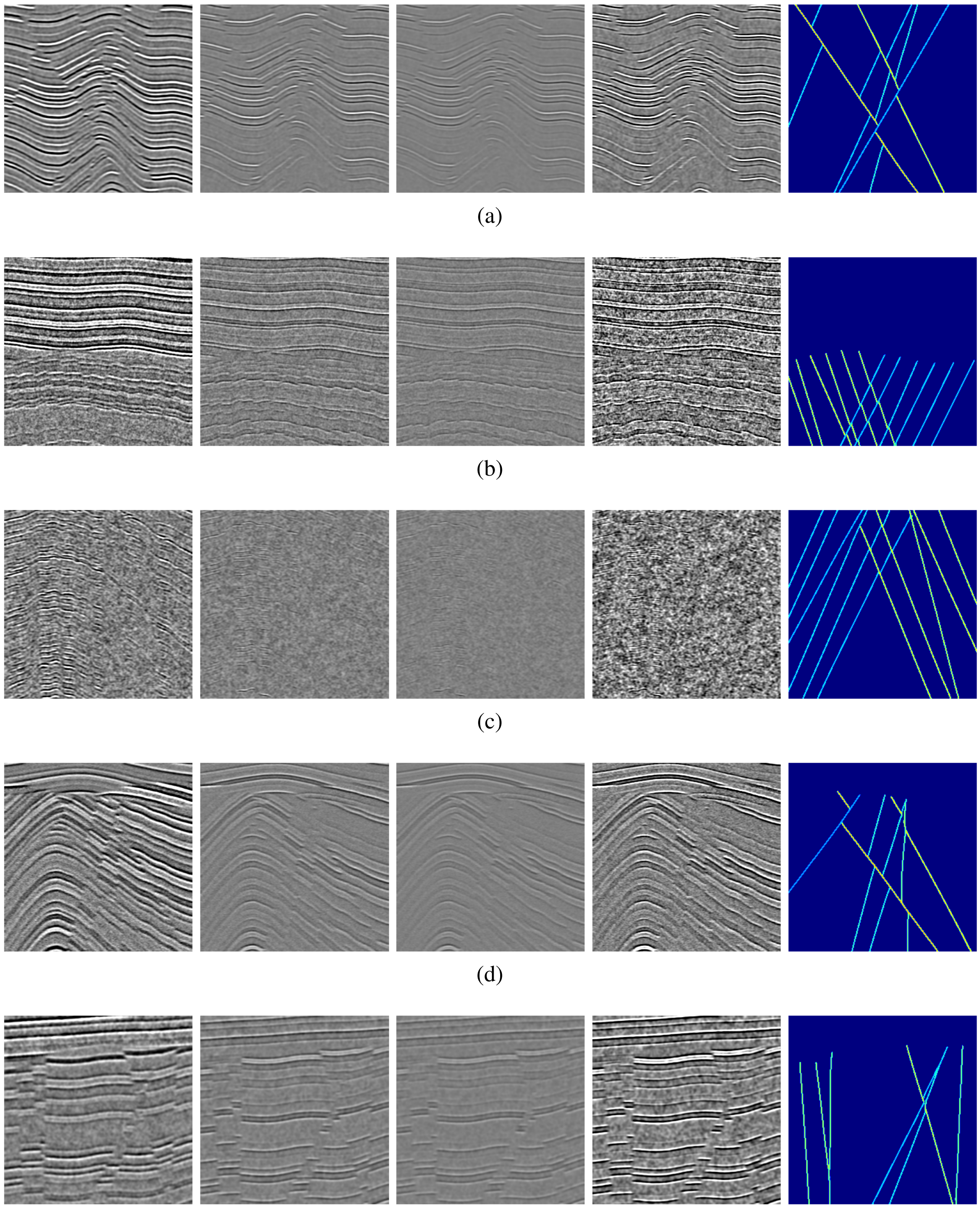

(a)

(b)

(c)

(d)

(e)

Figure 14: Five examples for validating 2D SCF-Net on elastic images. The first four columns represent PP, PS, SP, and SS images, respectively. The fifth column displays the fault dip images inferred by elastic SCF-Net.

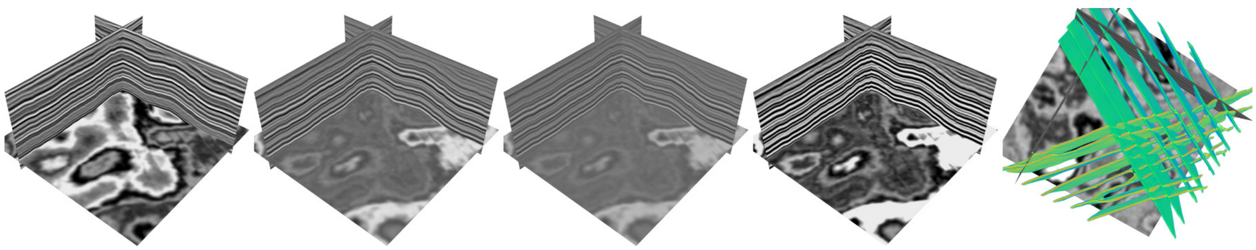

(a)

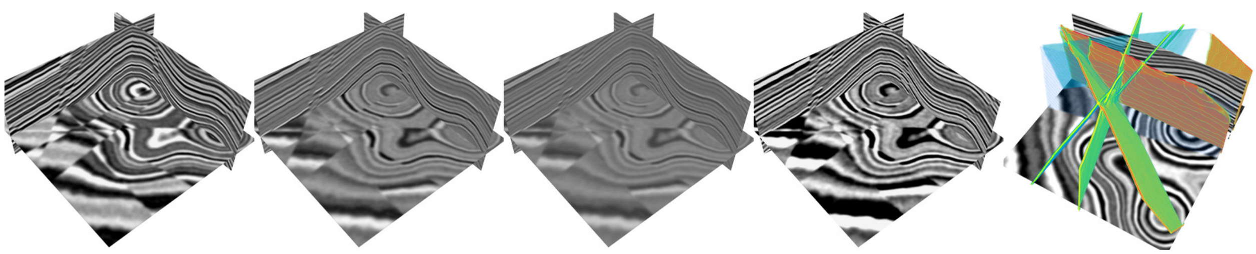

(b)

Figure 15: Two examples for validating 3D SCF-Net on elastic images. The first four columns represent PP, PS, SP, and SS images, respectively. The fifth column displays the the fault strike images inferred by elastic SCF-Net.